Constraining $\sum m_\nu$ with the Bispectrum I: Breaking Parameter Degeneracies

ChangHoon Hahn,[1,2,*] Francisco Villaescusa-Navarro,[3] Emanuele Castorina,[2,1] and Roman Scoccimarro[4]

[1]*Lawrence Berkeley National Laboratory, 1 Cyclotron Rd, Berkeley CA 94720, USA*
[2]*Berkeley Center for Cosmological Physics, University of California, Berkeley, CA 94720, USA*
[3]*Center for Computational Astrophysics, Flatiron Institute, 162 5th Avenue, New York, NY 10010, USA*
[4]*Center for Cosmology and Particle Physics, Department of Physics, New York University, NY 10003, New York, USA*

(Dated: `DRAFT --- 4c5cce0 --- 2019-04-04 --- NOT READY FOR DISTRIBUTION`)

ABSTRACT

abstract

Keywords: cosmology: —

1. INTRODUCTION

very brief into on neutrinos

Brief intro on the impact of massive active neutrinos on the matter powerspectrum and how that's detectable with CMB and LSS

Quick summary of current constraints and where they come from. Talk about the CMB-LSS lever arm. The degeneracy between As and tau and how that's a bottleneck short thing about how τ is hard to constrain.

Fortunately the imprint of neutrinos on the matter distribution leaves imprints on clustering. So with clustering measurements alone we can derive constraints on $\sum m_\nu$ and at the very least tighten constraints.

Brief summary of previous works that look at the powerspectrum. Then Discuss the shortcomings of the powerspectrum only analysis– Not good enough.

However, we don't have to settle for just two point statistics, three-point statistics such as the bispectrum and 3PCF...

In Section blah

CH: List plans for paper 2

2. HADES AND QUIJOTE SIMULATION SUITES

We use a subset of the HADES[1] and Quijote simulation suites. Below, we briefly describe these simulations; a brief summary of the simulations can be found in Table 1. The HADES simulations start from Zel'dovich approximated initial conditions generated at $z = 99$ using the Zennaro

---

[1] https://franciscovillaescusa.github.io/hades.html

et al. (2017) rescaling method and follow the gravitational evolution of $N_{\rm cdm} = 512^3$ CDM, plus $N_\nu = 512^3$ neutrino particles (for massive neutrino models), to $z = 0$. They are run using the GADGET-III TreePM+SPH code (Springel 2005) in a periodic $(1h^{-1}{\rm Gpc})^3$ box. All of the HADES simulations share the following cosmological parameter values, which are in good agreement with Planck constraints Ade et al. (2016): $\Omega_{\rm m}{=}0.3175, \Omega_{\rm b}{=}0.049, \Omega_\Lambda{=}0.6825, n_s{=}0.9624, h{=}0.6711$, and $k_{\rm pivot} = 0.05\ h{\rm Mpc}^{-1}$.

The HADES suite includes models with degenerate massive neutrinos of different masses: $\sum m_\nu = 0.06, 0.10$, and 0.15 eV. These massive neutrino models are run using the "particle method", where neutrinos are described as a collisionless and pressureless fluid and therefore modeled as particles, same as CDM (Brandbyge et al. 2008; Viel et al. 2010). HADES also includes models with massless neutrino and different values of σ_8 to examine the $\sum m_\nu - \sigma_8$ degeneracy. The σ_8 values were chosen to match either σ_8^m or σ_8^c — σ_8 computed with respect to total matter (CDM + baryons + ν) or CDM + baryons — of the massive neutrino models: $\sigma_8 = 0.822, 0.818, 0.807$, and 0.798. Each model has 100 independent realizations and we focus on the snapshots saved at $z = 0$. Halos closely trace the CDM+baryon field rather than the total matter field and neutrinos have negligible contribution to halo masses (*e.g.* Ichiki & Takada 2012; Castorina et al. 2014; LoVerde 2014; Villaescusa-Navarro et al. 2014). Hence, dark matter halos are identified in each realization using the Friends-of-Friends algorithm (FoF; Davis et al. 1985) with linking length $b = 0.2$ on the CDM + baryon distribution; only halos with masses $> 3.2 \times 10^{13} h^{-1} M_\odot$ are included. For further details on the HADES simulations, we refer readers to Villaescusa-Navarro et al. (2018).

In addition to HADES, we use simulations from the Quijote simulation suite, a set of 23,000 N-body simulations that in total contain more than 3.3 trillion (3.3×10^{12}) particles over a volume of $23000(h^{-1}{\rm Gpc})^3$. These simulations were constructed to quantify the information content of different cosmological observables using Fisher matrix forecasting (*e.g.* Section 4.2). They are therefore designed to accurately calculate the covariance matrices of observables and the derivatives of observables with respect to cosmological parameters. The suite considers 6 cosmological parameters: $\Omega_{\rm m}$, $\Omega_{\rm b}$, h, n_s, σ_8, and $\sum m_\nu$.

To calculate covariance matrices, Quijote includes 15,000 N-body simulations run at a fiducial cosmology ($\Omega_{\rm m}{=}0.3175$, $\Omega_{\rm b}{=}0.049$, $h{=}0.6711$, $n_s{=}0.9624$, $\sigma_8{=}0.834$, and $\sum m_\nu{=}0.0$ eV). It also includes sets of 500 N-body simulations run at different cosmologies where only one parameter is varied from the fiducial cosmology at a time for the derivatives. Along $\Omega_{\rm m}$, $\Omega_{\rm b}$, h, n_s, and σ_8, the fiducial cosmology is adjusted by either a small step above and below the fiducial value. Along $\sum m_\nu$, because the derivative of certain observable with respect to $\sum m_\nu$ is noisy, Quijote includes sets of 500 simulations for $\sum m_\nu = 0.1, 0.2$, and 0.4 eV. In Table 1, we list the cosmologies included in the Quijote suite.

The intial conditions for all Quijote simulations were generated at $z = 127$ using 2LPT for simulations with massless neutrinos and the Zel'dovich approximation for massive neutrinos. Like HADES, the initial conditions of simulations with massive neutrinos take their scale-dependent growth factors/rates into account using the Zennaro et al. (2017) method. From the initial conditions, all of the simulations follow the gravitational evolution of 512^3 dark matter particles, and 512^3 neutrino
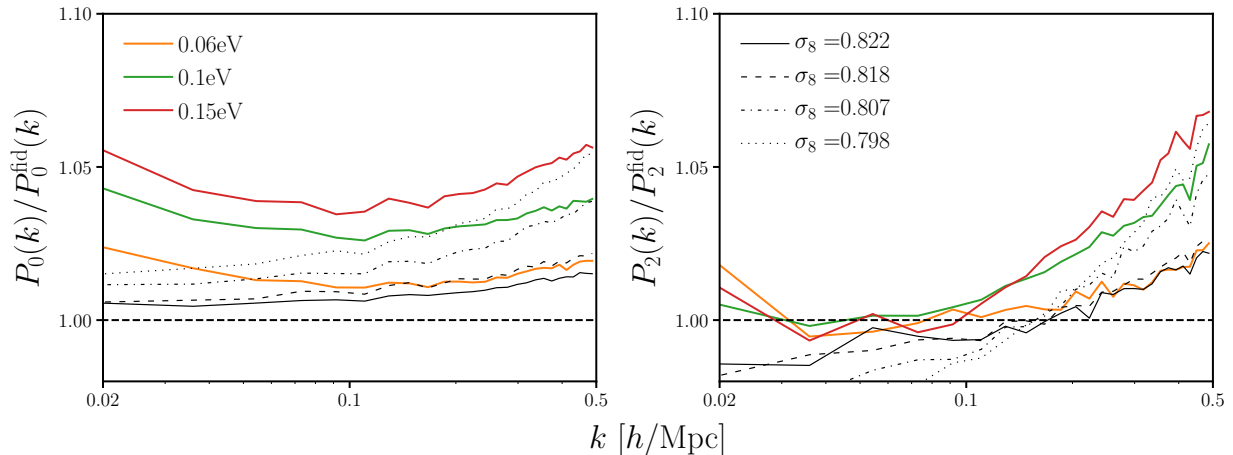
Figure 1. Impact of $\sum m_\nu$ and σ_8 on the redshift-space halo power spectrum monopole and quadrupole measured using the HADES simulation suite. $\sum m_\nu$ and σ_8 produce almost identical effects on halo clustering on small scales ($k > 0.1\,h/\mathrm{Mpc}$). This degeneracy can be partially broken through the quadrupole; however, *$\sum m_\nu$ and σ_8 produce almost the same effect on two-point clustering — within a few percent.*

particles (for massive neutrino models), to $z = 0$. The simulations run at the fiducial cosmology for covariance matrix estimation are standard N-body simulations. However, the rest are paired fixed simulations, which greatly reduce cosmic variance without introducing bias for a large set of statistics (Angulo & Pontzen 2016; Pontzen et al. 2016; Villaescusa-Navarro et al. 2018). We confirm that the paired fixed simulations do not introduce any bias for the redshift-space halo bispectrum (the observable we considered in this paper). For further details on the Quijote simulations, we refer readers to Villaescusa-Navarro et al. (in preparation).

3. BISPECTRUM

We're interested in breaking parameter degeneracies that limit the constraining power on $\sum m_\nu$ of two-point clustering analyses using three-point clustering statistics — *i.e.* the bispectrum. In this section, we describe the bispectrum estimator used throughout the paper. We focus on the bispectrum monopole ($\ell = 0$) and use an estimator that exploits Fast Fourier Transpforms (FFTs). Our estimator is similar to the estimators described in Scoccimarro (2015); Sefusatti et al. (2016); we also follow their formalism in our description below. Although Sefusatti et al. (2016) and Scoccimarro (2015) respectively describe estimators in redshift- and real-space, since we focus on the bispectrum monopole, we note that there is no difference.

To measure the bispectrum of our halo catalogs, we begin by interpolating the halo positions to a grid, $\delta(\boldsymbol{x})$ and Fourier transforming the grid to get $\delta(\boldsymbol{k})$. We use a fourth-order interpolation to interlaced grids, which has advantageous anti-aliasing properties (Hockney & Eastwood 1981; Sefusatti et al. 2016) that allow unbias measurements up to the Nyquist frequency. Then using $\delta(\boldsymbol{k})$, we measure the bispectrum monopole as

$$\widehat{B}_{\ell=0}(k_1, k_2, k_3) = \frac{1}{V_B} \int_{k_1} \mathrm{d}^3 q_1 \int_{k_2} \mathrm{d}^3 q_2 \int_{k_3} \mathrm{d}^3 q_3 \, \delta_\mathrm{D}(\boldsymbol{q}_{123}) \, \delta(\boldsymbol{q}_1) \, \delta(\boldsymbol{q}_2) \, \delta(\boldsymbol{q}_3) - B_{\ell=0}^\mathrm{SN} \tag{1}$$

Table 1. Specifications of the HADES and Quijote simulation suites.

Name	$\sum m_\nu$ (eV)	Ω_m	Ω_b	h	n_s	σ_8^m	σ_8^c	$m_{\rm cdm}$ $(10^{10}h^{-1}M_\odot)$	m_ν $(10^{10}h^{-1}M_\odot)$	realizations
					HADES suite					
Fiducial	0.0	0.3175	0.049	0.6711	0.9624	0.833	0.833	65.66	0	100
	0.06	0.3175	0.049	0.6711	0.9624	0.819	0.822	65.36	29.57	100
	0.10	0.3175	0.049	0.6711	0.9624	0.809	0.815	65.16	49.28	100
	0.15	0.3175	0.049	0.6711	0.9624	0.798	0.806	64.92	73.95	100
	0.0	0.3175	0.049	0.6711	0.9624	0.822	0.822	65.66	0	100
	0.0	0.3175	0.049	0.6711	0.9624	0.818	0.818	65.66	0	100
	0.0	0.3175	0.049	0.6711	0.9624	0.807	0.807	65.66	0	100
	0.0	0.3175	0.049	0.6711	0.9624	0.798	0.798	65.66	0	100
					Qujiote suite					
Fiducial	0.0	0.3175	0.049	0.6711	0.9624	0.834	0.834			15,000
$\sum m_\nu^+$	0.1	0.3175	0.049	0.6711	0.9624	0.834	0.834			500
$\sum m_\nu^{++}$	0.2	0.3175	0.049	0.6711	0.9624	0.834	0.834			500
$\sum m_\nu^{+++}$	0.4	0.3175	0.049	0.6711	0.9624	0.834	0.834			500
Ω_m^+	0.0	0.3275	0.049	0.6711	0.9624	0.834	0.834			500
Ω_m^-	0.0	0.3075	0.049	0.6711	0.9624	0.834	0.834			500
Ω_b^+	0.0	0.3175	0.050	0.6711	0.9624	0.834	0.834			500
Ω_b^-	0.0	0.3175	0.048	0.6711	0.9624	0.834	0.834			500
h^+	0.0	0.3175	0.049	0.6911	0.9624	0.834	0.834			500
h^-	0.0	0.3175	0.049	0.6511	0.9624	0.834	0.834			500
n_s^+	0.0	0.3175	0.049	0.6711	0.9824	0.834	0.834			500
n_s^-	0.0	0.3175	0.049	0.6711	0.9424	0.834	0.834			500
σ_8^+	0.0	0.3175	0.049	0.6711	0.9624	0.849	0.849			500
σ_8^-	0.0	0.3175	0.049	0.6711	0.9624	0.819	0.819			500

Notes: CH: description of the table

$\delta_{\rm D}$ above is a Dirac delta function and hence $\delta_{\rm D}(\boldsymbol{q}_{123}) = \delta_{\rm D}(\boldsymbol{q}_1 + \boldsymbol{q}_2 + \boldsymbol{q}_3)$ ensures that the $\boldsymbol{q}_i$ triplet actually form a closed triangle. Each of the integrals above represent an integral over a spherical shell in k-space with radius δk centered at $\boldsymbol{k}_i$ — $i.e.$

$$\int_{k_i} {\rm d}^3 q \equiv \int_{k_i - \delta k/2}^{k_i + \delta k/2} {\rm d}q \; q^2 \int {\rm d}\Omega. \tag{2}$$
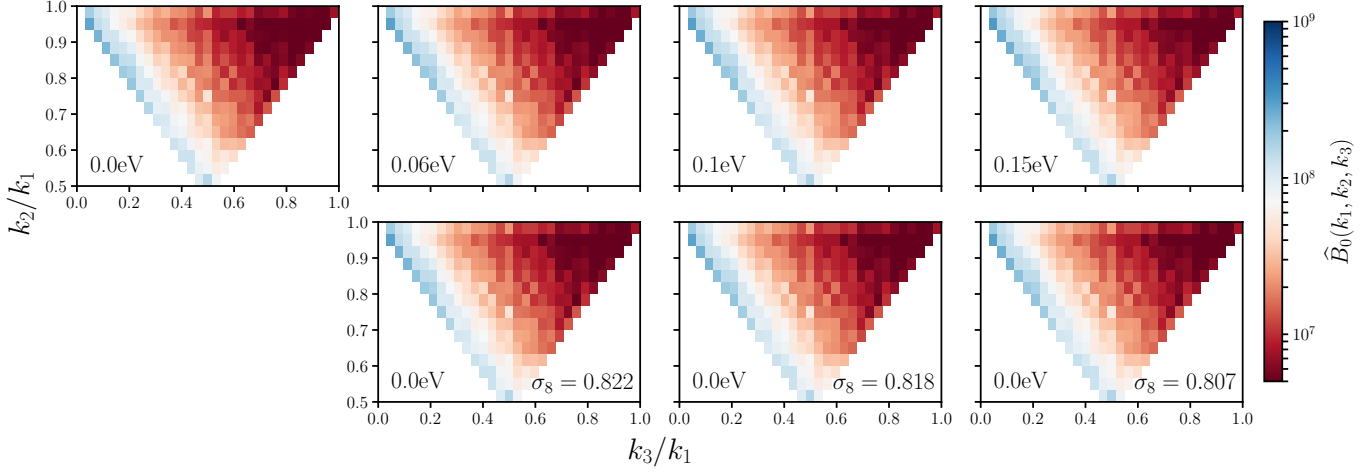
Figure 2. The redshift-space halo bispectrum, $\widehat{B}_0(k_1, k_2, k_3)$, as a function of triangle configuration shape for $\sum m_\nu = 0.0, 0.06, 0.10,$ and $0.15\,\text{eV}$ (upper panels) and $\sigma_8 = 0.822, 0.818,$ and 0.807 (lower panels). The HADES simulations of the top and bottom panels in the three right-most columns, have matching σ_8 values (Section 2). We describe the triangle configuration shape by the ratio of the triangle sides: k_3/k_1 and k_2/k_1. The upper left bin contains squeezed triangles ($k_1 = k_2 \gg k_3$); the upper right bin contains equilateral triangles ($k_1 = k_2 = k_3$); and the bottom center bin contains folded triangles ($k_1 = 2k_2 = 2k_3$). We include all triangle configurations with $k_1, k_2, k_3 \leq k_{\max} = 0.5\,h/\text{Mpc}$. and use the $\widehat{B}_0$ estimator in Section 3.

V_B is a normalization factor proportional to the number of triplets $\boldsymbol{q}_1$, $\boldsymbol{q}_2$, and $\boldsymbol{q}_3$ that can be found in the triangle bin defined by k_1, k_2, and k_3 with width δk:

$$V_B = \int_{k_1} \mathrm{d}^3 q_1 \int_{k_2} \mathrm{d}^3 q_2 \int_{k_3} \mathrm{d}^3 q_3 \; \delta_{\mathrm{D}}(\boldsymbol{q}_{123}) \tag{3}$$

Lastly, $B_{\ell=0}^{\mathrm{SN}}$ is the correction for the Poisson shot noise, which contributes due to the self-correlation of individual objects:

$$B_{\ell=0}^{\mathrm{SN}}(k_1, k_2, k_3) = \frac{1}{\bar{n}}\big(P_0(k_1) + P_0(k_2) + P_0(k_3)\big) + \frac{1}{\bar{n}^2}. \tag{4}$$

$\bar{n}$ is the number density of objects (halos) and P_0 is the powerspectrum monopole.
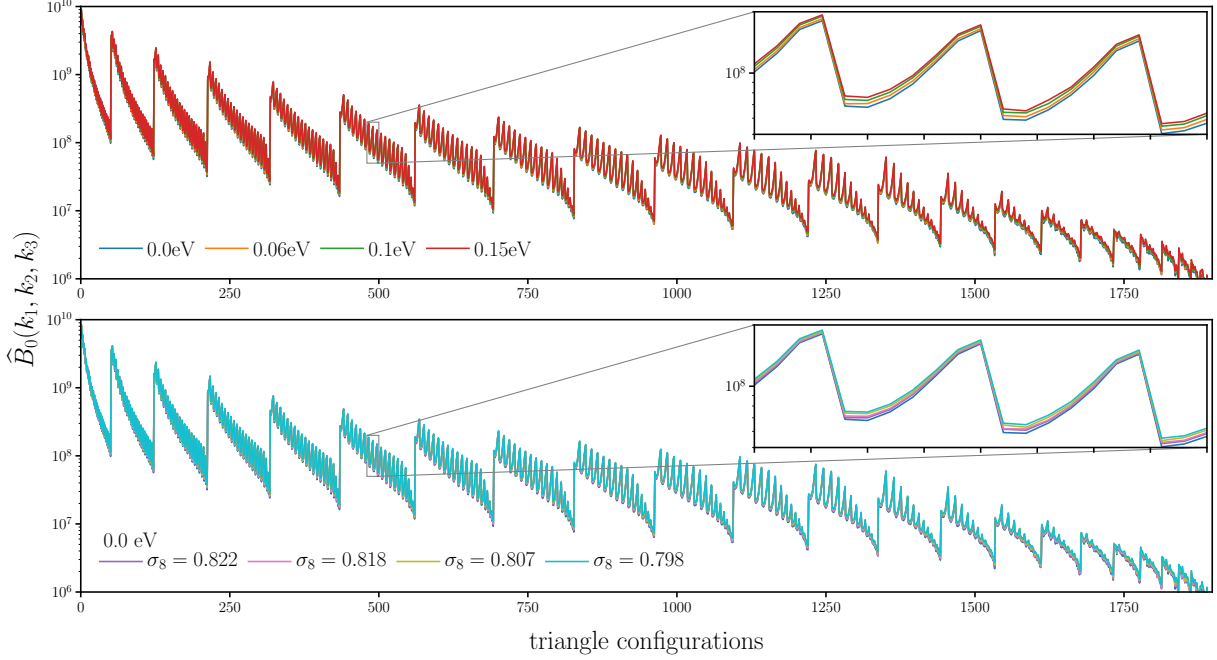
In order to evaluate the integrals in Eq. 1, we take advantage of the plane-wave representation of the Dirac delta function and rewrite the equation as

$$\widehat{B}_{\ell=0}(k_1, k_2, k_3) = \frac{1}{V_B} \int \frac{\mathrm{d}^3 x}{(2\pi)^3} \int_{k_1} \mathrm{d}^3 q_1 \int_{k_2} \mathrm{d}^3 q_2 \int_{k_3} \mathrm{d}^3 q_3 \; \delta(\boldsymbol{q}_1)\,\delta(\boldsymbol{q}_2)\,\delta(\boldsymbol{q}_3)\,e^{i\boldsymbol{q}_{123}\cdot\boldsymbol{x}} - B_{\ell=0}^{\mathrm{SN}} \tag{5}$$

$$= \frac{1}{V_B} \int \frac{\mathrm{d}^3 x}{(2\pi)^3} \prod_{i=1}^{3} I_{k_i}(\boldsymbol{x}) - B_{\ell=0}^{\mathrm{SN}} \tag{6}$$

where

$$I_{k_i}(\boldsymbol{x}) = \int_{k} \mathrm{d}^3 q \; \delta(\boldsymbol{q})\, e^{i\boldsymbol{q}\cdot\boldsymbol{x}}. \tag{7}$$
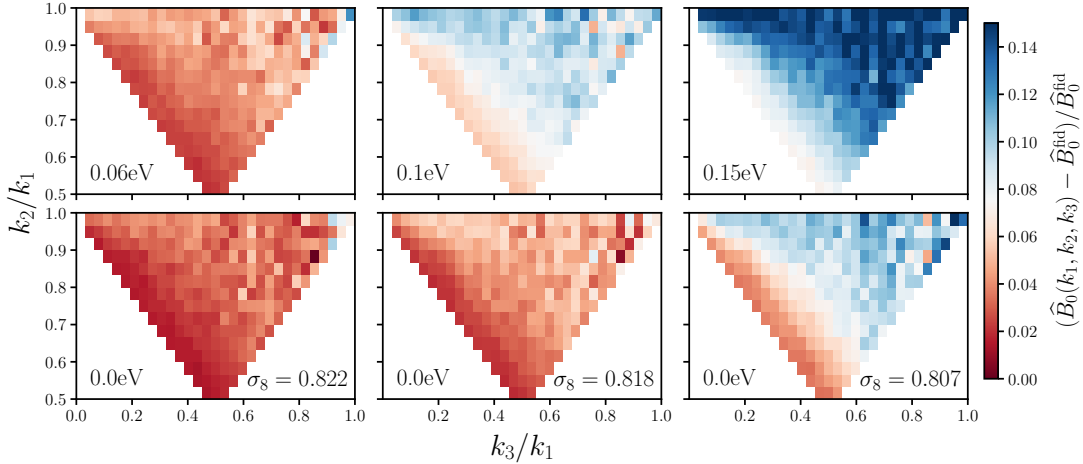
Figure 3. The redshift-space halo bispectrum, $\widehat{B}_0(k_1, k_2, k_3)$, as a function of triangle configurations for $\sum m_\nu = 0.0, 0.06, 0.10$, and $0.15\,\mathrm{eV}$ (top panel) and $\sum m_\nu = 0.0\,\mathrm{eV}$, $\sigma_8 = 0.822, 0.818, 0.807$, and 0.798 (lower panel). We include all possible triangle configurations with $k_1, k_2, k_3 \leq k_{\max} = 0.5\,h/\mathrm{Mpc}$ where we order the configurations by looping through k_3 in the inner most loop and k_1 in the outer most loop satisfying $k_1 \leq k_2 \leq k_3$. In the insets of the panels we zoom into triangle configurations with $k_1 = 0.113$, $0.226 \leq k_2 \leq 0.283$, and $0.283 \leq k_3 \leq 0.377\,h/\mathrm{Mpc}$.

At this point, we measure $\widehat{B}_{\ell=0}(k_1, k_2, k_3)$ by calcuating the I_{k_i}s with inverse FFTs and summing over in real space.[2] For $\widehat{B}_{\ell=0}$ measurements throughout the paper, we use $\delta(\boldsymbol{x})$ grids with $N_{\mathrm{grid}} = 360$ and triangle configurations defined by k_1, k_2, k_3 bins of width $\Delta k = 3k_f = 0.01885\,h/\mathrm{Mpc}$.

We present the redshift-space halo bispectrum of the HADE simulations measured using the estimator above in two ways: one that emphasizes the triangle shape dependence (Figure 2) and the other that emphasizes the amplitude (Figure 3). In Figure 2, we plot $\widehat{B}_0(k_1, k_2, k_3)$ as a function of k_2/k_1 and k_3/k_1, which describe the triangle configuration shape. In each panel, the colormap in each $(k_2/k_1, k_3/k_1)$ bin is the weighted average $\widehat{B}_0$ amplitude of all triangle configurations in the bin. The upper left bins contain squeezed triangles ($k_1 = k_2 \gg k_3$); the upper right bins contain equilateral triangles ($k_1 = k_2 = k_3$); and the bottom center bins contain folded triangles ($k_1 = 2k_2 = 2k_3$). We include all possible triangle configurations with $k_1, k_2, k_3 < k_{\max} = 0.5\,h/\mathrm{Mpc}$. The $\widehat{B}_0$ in the upper panels are HADES models with $\sum m_\nu = 0.0$ (fiducial), $0.06, 0.10$, and $0.15\,\mathrm{eV}$; $\widehat{B}_0$ in the lower panels are HADES models with $\sum m_\nu 0.0\,\mathrm{eV}$ and $\sigma_8 = 0.822, 0.818$, and 0.807. The top and bottom panels of the three right-most columns have matching σ_8 values (Section 2).

---

[2] The code that we use to evaluate $\widehat{B}_{\ell=0}$ is publicly available at https://github.com/changhoonhahn/pySpectrum

Figure 4. The shape dependence of the $\sum m_\nu$ and σ_8 imprint on the redshift-space halo bispectrum, $\Delta\widehat{B}_0/\widehat{B}_0^{\rm fid}$. We align the $\sum m_\nu = 0.06, 0.10$, and $0.15\,{\rm eV}$ HADES models in the upper panels with $\sum m_\nu = 0.0$ eV $\sigma_8 = 0.822, 0.818$, and 0.807 models on the bottom such that the top and bottom panels in each column have matching σ_8^c, which produce mostly degenerate imprints on the redshift-space power spectrum. The difference between the top and bottom panels highlight that $\sum m_\nu$ leaves a distinct imprint on elongated and isosceles triangles (bins along the bottom left and bottom right edges, respectively) from σ_8. *The imprint of $\sum m_\nu$ has an overall distinct shape dependence on the bispectrum that cannot be replicated by varying σ_8.*

Next, in Figure 3, we plot $\widehat{B}_0(k_1, k_2, k_3)$ for all possible triangle configurations with $k_1, k_2, k_3 < k_{\rm max} = 0.5\ h/{\rm Mpc}$ where we order the configurations by looping through k_3 in the inner most loop and k_1 in the outer most loop with $k_1 \leq k_2 \leq k_3$. In the top panel, we present $\widehat{B}_0$ of HADES models with $\sum m_\nu = 0.0, 0.06, 0.10$, and $0.15\,{\rm eV}$; in the lower panel, we present $\widehat{B}_0$ of HADES models with $\sum m_\nu 0.0$ eV and $\sigma_8 = 0.822, 0.818$, and 0.807. We zoom into triangle configurations with $k_1 = 0.113$, $0.226 \leq k_2 \leq 0.283$, and $0.283 \leq k_3 \leq 0.377\ h/{\rm Mpc}$ in the insets of the panels.

4. RESULTS

4.1. *Breaking the $\sum m_\nu - \sigma_8$ degeneracy*

One major bottleneck of constraining $\sum m_\nu$ with the power spectrum alone is the strong $\sum m_\nu$ – σ_8 degeneracy. The imprint of $\sum m_\nu$ and σ_8 on the power spectrum are degenerate and for models with the same σ_8^c, the power spectrum only differ by $< 1\%$ (see Figure 1 and Villaescusa-Navarro et al. 2018). The HADES suite, which has simulations with $\sum m_\nu = 0.0, 0.06, 0.10$, and 0.15 eV as well as $\sum m_\nu = 0.0$ eV simulations with matching σ_8^c — $\sigma_8 = 0.822, 0.818$, and 0.807 , provide an ideal set of simulations to separate the impact of $\sum m_\nu > 0.0$ eV and examine the degeneracy between $\sum m_\nu$ and σ_8 (Section 2 and Table 1). Hence, by measuring bispectrum of these simulations (Figure 2 and 3), we can determine whether the bispectrum helps break the $\sum m_\nu - \sigma_8$ degeneracy. Below, we present our comparison of the HADES bispectrum and illustrate that the bispectrum can significantly improve $\sum m_\nu$ constraints by breaking the $\sum m_\nu - \sigma_8$ degeneracy.

We begin by examining the triangle shape dependent imprint of $\sum m_\nu$ on the redshift-space halo bispectrum versus σ_8 alone. In Figure 4, we present the fractional residual, $(\Delta\widehat{B}_0 = \widehat{B}_0 - \widehat{B}_0^{\rm fid})/\widehat{B}_0^{\rm fid}$,
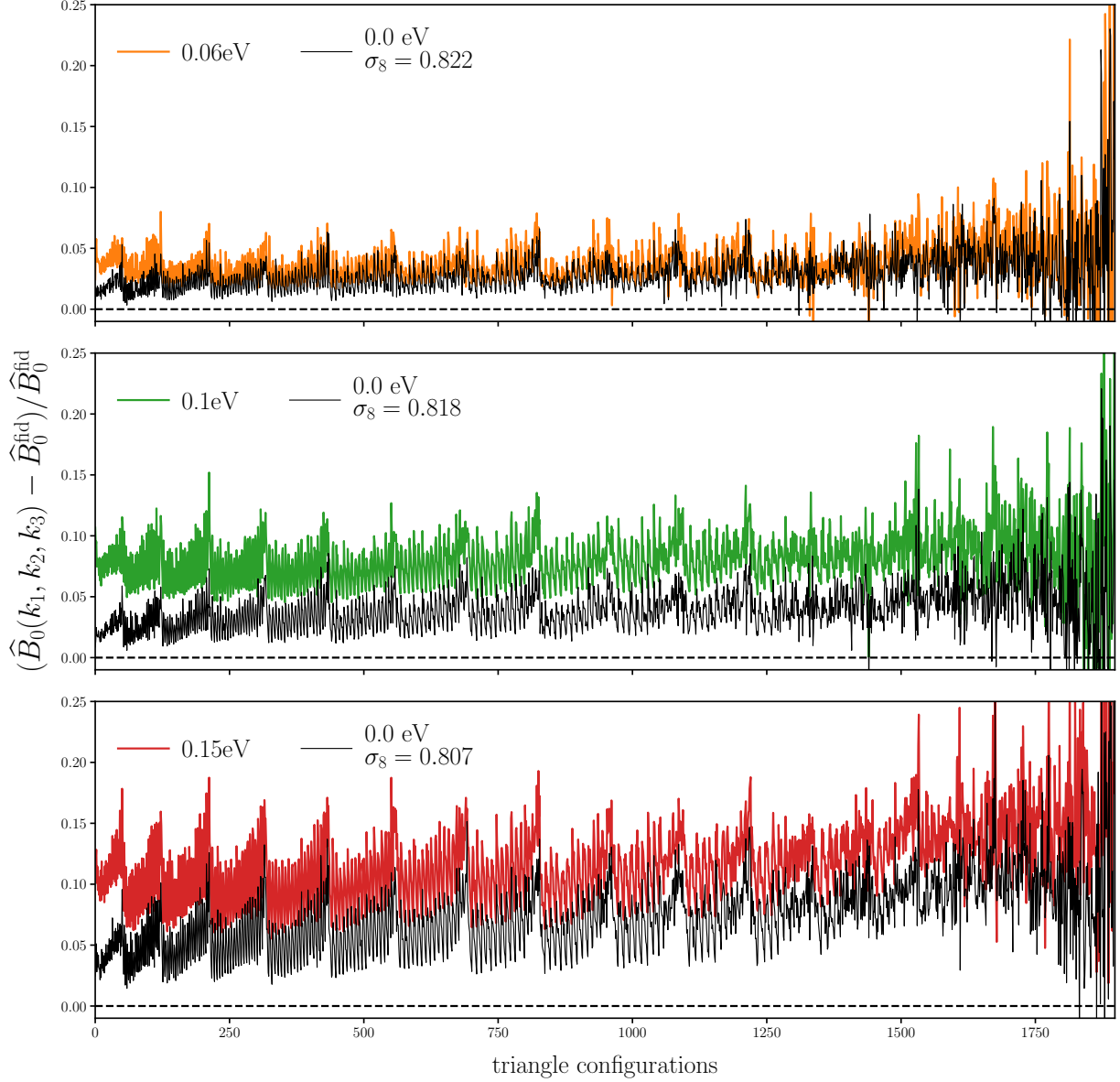
Figure 5. The impact of $\sum m_\nu$ and σ_8 on the redshift-space halo bispectrum, $\Delta\widehat{B}_0/\widehat{B}_0^{\rm fid}$, for all 1898 triangle configurations with $k_1, k_2, k_3 \leq 0.5h/{\rm Mpc}$. We compare $\Delta\widehat{B}_0/\widehat{B}_0^{\rm fid}$ of the $\sum m_\nu = 0.06$ (top), 0.10 (middle), and 0.15 eV (bottom) HADES models to $\Delta\widehat{B}_0/\widehat{B}_0^{\rm fid}$ of $\sum m_\nu = 0.0$ eV $\sigma_8 = 0.822$, 0.818, and 0.807 models. The impact of $\sum m_\nu$ on the bispectrum has a significantly different amplitude than the impact of σ_8. For instance, $\sum m_\nu = 0.15$ eV (red) has a $\sim 5\%$ stronger impact on the bispectrum than $\sum m_\nu = 0.0$ eV $\sigma_8 = 0.798$ (black) even though their powerspectrums only differ by $< 1\%$ (Figure 1). Combined with the different shape-dependence (Figure 4), *the distinct imprint of $\sum m_\nu$ on the bispectrum illustrate that the bispectrum can break the degeneracy between $\sum m_\nu$ and σ_8 that degrade constraints from two-point analyses.*

as a function of k_2/k_1 and k_3/k_1 for $\sum m_\nu = 0.06, 0.10$, and 0.15 eV in the upper panels and 0.0 eV $\sigma_8 = 0.822$, 0.818, and 0.807 in the bottom panels. The simulations in the top and bottom panels of each column have matching σ_8^c. Overall as $\sum m_\nu$ increases, the bispectrum for increases for all triangle

shapes (top panels). For triangle shapes close to equilateral (upper right) and squeezed (upper left), the increase is significantly larger. For $\sum m_\nu = 0.15$ eV, the bispectrum is $\sim 15\%$ higher than $\widehat{B}_0^{\mathrm{fid}}$ for equilateral and squeezed triangles. Meanwhile, the bispectrum increases by $\sim 8\%$ for folded triangles (lower center).

As σ_8 increases, with $\sum m_\nu = 0.0$ eV fixed, the bispectrum increases overall for all triangle shapes (bottom panels). However, the comparison of the top and bottom panels in each column reveals significant differences in $\Delta \widehat{B}_0/\widehat{B}_0^{\mathrm{fid}}$ for $\sum m_\nu$ versus σ_8 alone. Between $\sum m_\nu = 0.15$ eV and 0.0 eV $\sigma_8 = 0.807$, there is an overall $\gtrsim 5\%$ difference. In addition, the shape dependence of the $\Delta \widehat{B}_0/\widehat{B}_0^{\mathrm{fid}}$ increase is different for $\sum m_\nu$ than σ_8. This is particularly clear in the differences between 0.1 eV (top center panel) and 0.0 eV and $\sigma_8 = 0.807$ (bottom right panel): near equilateral triangles in the two panels have similar $\Delta \widehat{B}_0/\widehat{B}_0^{\mathrm{fid}}$ while triangle shapes near the lower left edge from the squeezed to folded triangles have significantly different $\Delta \widehat{B}_0/\widehat{B}_0^{\mathrm{fid}}$. Hence, $\sum m_\nu$ leaves an imprint on the bispectrum with a distinct triangle shape dependence than σ_8 alone. In other words, unlike the power spectrum, the triangle shape dependent impact of $\sum m_\nu$ on the bispectrum cannot be replicated by varying σ_8.

We next examine the amplitude of the $\sum m_\nu$ imprint on the redshift-space halo bispectrum versus σ_8 alone for all triangle configurations. We present $\Delta \widehat{B}_0/\widehat{B}_0^{\mathrm{fid}}$ for all 1898 possible triangle configurations with $k_1, k_2, k_3 < k_{\mathrm{max}} = 0.5$ h/Mpc in Figure 5. We compare $\Delta \widehat{B}_0/\widehat{B}_0^{\mathrm{fid}}$ of the $\sum m_\nu = 0.06, 0.10,$ and 0.15 eV HADES models to the $\Delta \widehat{B}_0/\widehat{B}_0^{\mathrm{fid}}$ of $\sum m_\nu = 0.0$ eV $\sigma_8 = 0.822, 0.818,$ and 0.807 models in the top, middle, and bottom panels, respectively. The comparison confirms the overall amplitude difference between $\sum m_\nu$ and σ_8 (Figure 4). For instance, $\sum m_\nu = 0.15$ eV (red) has a $\sim 5\%$ stronger impact on the bispectrum than $\sum m_\nu = 0.0$ eV $\sigma_8 = 0.798$ (black) even though their power spectrums differ by $< 1\%$ (Figure 1).

The comparison in the panels of Figure 5 also reveal a difference in the configuration dependence in $\Delta \widehat{B}_0/\widehat{B}_0^{\mathrm{fid}}$ of $\sum m_\nu$ versus σ_8. The triangle configurations are ordered by looping through k_3 in the inner most loop and k_1 in the outer most loop such that $k_1 \leq k_2 \leq k_3$. In this ordering, k_1 increases from left to right. So $\Delta \widehat{B}_0/\widehat{B}_0^{\mathrm{fid}}$ of $\sum m_\nu$ has a smaller k_1 dependence than $\Delta \widehat{B}_0/\widehat{B}_0^{\mathrm{fid}}$ of σ_8. Combined with the different shape-dependence (Figure 4), the distinct imprint of $\sum m_\nu$ on the redshift-space halo bispectrum illustrates that the bispectrum can break the degeneracy between $\sum m_\nu$ and σ_8. Moreover it illustrates that by including the bispectrum, we can more precisely constrain $\sum m_\nu$ than with the power spectrum alone.

CH: comparison to Ruggeri et al. (2018) and literature

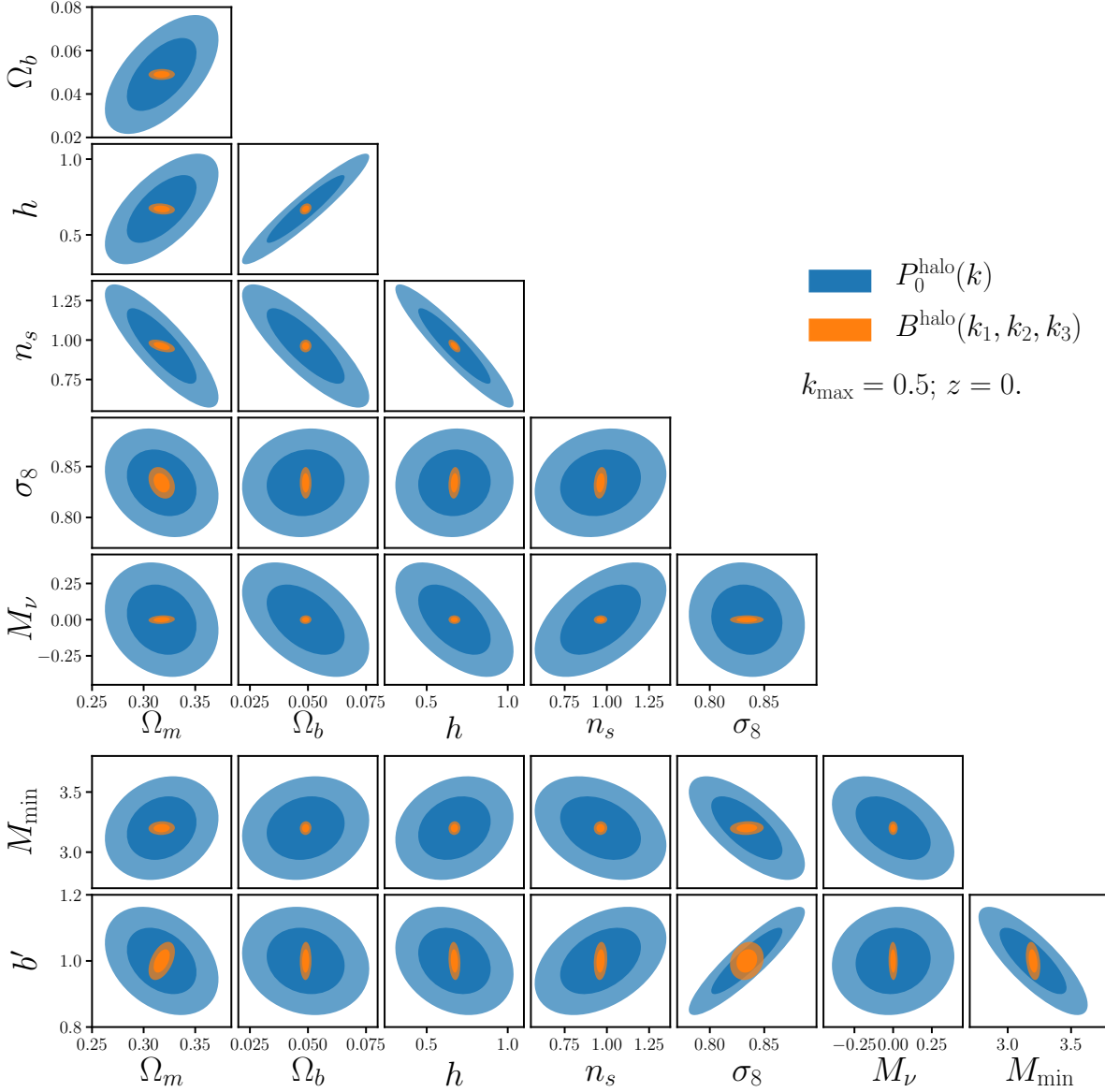## 4.2. $\sum m_\nu$ and other Cosmological Parameter Forecasts

We demonstrate in the previous section with the HADES simulations, that the bispectrum helps break the $\sum m_\nu$–σ_8 degeneracy, a major challenge in precisely constraining $\sum m_\nu$ with the power spectrum. This establishes the bispectrum as a promising probe for $\sum m_\nu$. However, we are ultimately interested in determining the constraining power of the bispectrum for an analysis that include cosmological parameters beyond $\sum m_\nu$ and σ_8— *i.e.* Ω_{m}, Ω_{b}, h, and n_s. The Quijote suite of simulations is *specifically* designed to answer this question using Fisher matrix forecast.
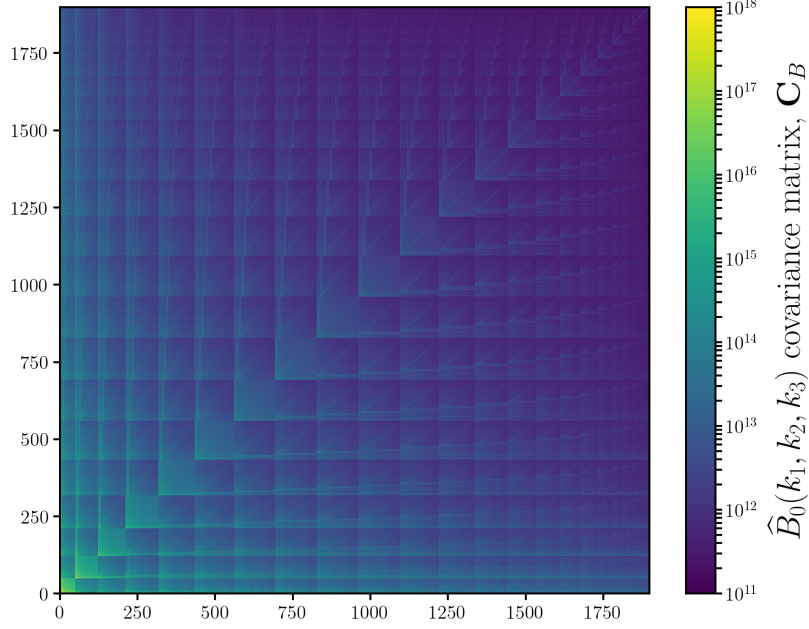
Figure 6. Covariance matrix of the redshift-space halo bispectrum estimated using the 15,000 realizations of the Qujiote simulation suite at the fiducial cosmology: Ω_m=0.3175, Ω_b=0.049, h=0.6711, n_s=0.9624, σ_8=0.834, and $\sum m_\nu$=0.0 eV. We include all possible triangle configurations with $k_1, k_2, k_3 < k_\mathrm{max} = 0.5$ h/Mpc and order the configurations (bins) in the same way as Figures 3 and 5. We use the covariance matrix above for the Fisher matrix forecasts presented in Section 4.2.

Table 2. Cosmological parameter constraints from the redshift-space halo power spectrum (top) and bispectrum (bottom).

	k_max (h/Mpc)	$\sum m_\nu$ (eV)	Ω_m	Ω_b	h	n_s	σ_8	b'	M_min ($10^{13}h^{-1}M_\odot$)
		0.0	0.3175	0.049	0.6711	0.9624	0.834	1.	3.2
P_0	0.2	$\pm$	$\pm$	$\pm$	$\pm$	$\pm$	$\pm$	$\pm$	$\pm$
	0.3	$\pm$	$\pm$	$\pm$	$\pm$	$\pm$	$\pm$	$\pm$	$\pm$
	0.4	$\pm$	$\pm$	$\pm$	$\pm$	$\pm$	$\pm$	$\pm$	$\pm$
	0.5	±0.319	±0.0444	±0.0221	±0.294	±0.315	±0.0430	±0.35	±0.13
B_0	0.2	$\pm$	$\pm$	$\pm$	$\pm$	$\pm$	$\pm$	$\pm$	$\pm$
	0.3	$\pm$	$\pm$	$\pm$	$\pm$	$\pm$	$\pm$	$\pm$	$\pm$
	0.4	$\pm$	$\pm$	$\pm$	$\pm$	$\pm$	$\pm$	$\pm$	$\pm$
	0.5	±0.0239	±0.0103	±0.00202	±0.0295	±0.0321	±0.0125	±0.046	±0.047

Figure 7. Fisher matrix constraints for $\sum m_\nu$ and other cosmological parameters for the redshift-space halo bispectrum monopole (orange). For comparison, we include Fisher parameter constraints for the redshift-space halo powerspectrum monopole in blue. The contours mark the 68% and 95% confidence interals. We set $k_{\mathrm{max}} = 0.5$ $h/$Mpc for both power spectrum and bispectrum. We include in our forecasts b' and M_{min}, a free amplitude scaling factor and halo mass limit, respectively. They serve as a simplistic bias model and we marginalize over them to that our constraints do not include extra constraining power from the difference in bias/number density in the different Quijote cosmologies. The bispectrum *substantially* improves constraints on all of the cosmological parameters over the power spectrum. *For $\sum m_\nu$, the bispectrum improves the constraint from $\sigma_{\sum m_\nu} = 0.319$ to 0.0239 eV — over an order of magnitude improvement over the power spectrum.*
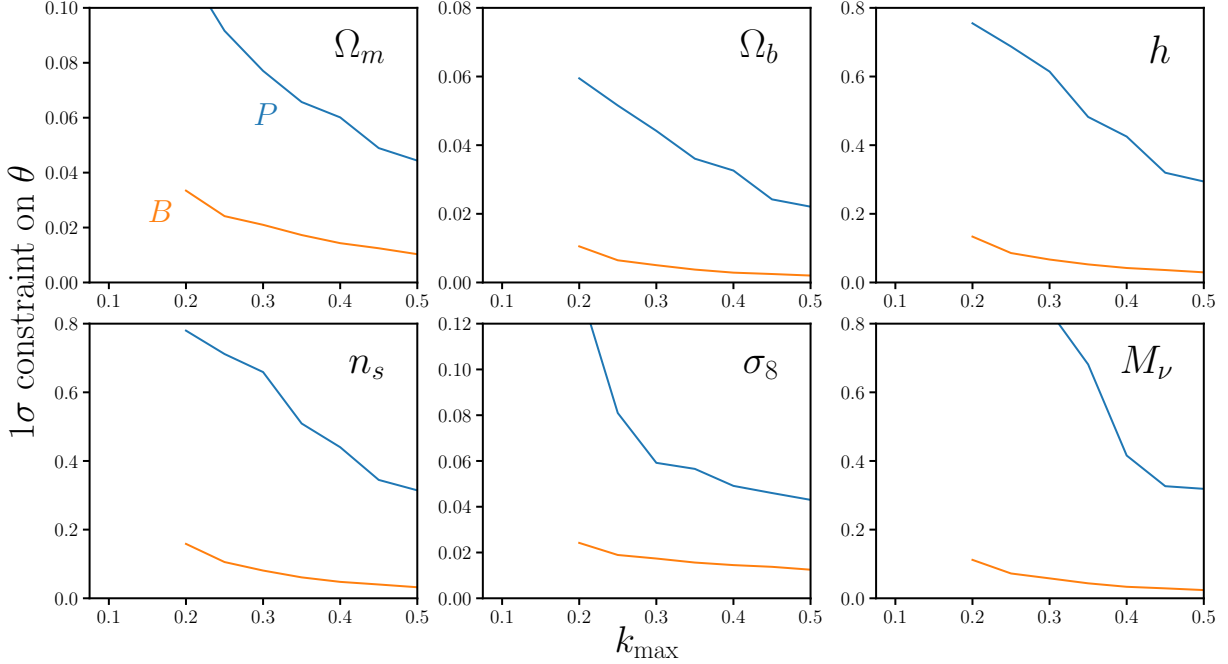
Figure 8. Marginalized 1σ constraints of Ω_m, Ω_b, h, n_s, σ_8, and $\sum m_\nu$ as a function of $k_{\max}$ for the redshift-space halo bispectrum (orange) and power spectrum (blue). Though not included in the figure, we marginalize over b' and $M_{\min}$ in our forecast.**CH:** more

First, the Quijote suite includes $15,000$ realizations run at a fiducial cosmology: $\sum m_\nu$=0.0eV, Ω_m=0.3175, Ω_b=0.049, n_s=0.9624, h=0.6711, and $\sigma_8 = 0.834$ (see Table 1. This allows us to robustly estimate the covariance matrix of the bispectrum, $\boldsymbol{C}$, which has $\sim 1,800$ triangle configurations (Figure 6). Second, the Quijote suite includes 500 fixed-pair realizations evaluated at 13 different cosmologies, each a small step away from the fiducial cosmology parameter values along one parameter (Section 2 and Table 1). These realizations allow us to precisely estimate the derivatives of the bispectrum with respect to each of the cosmological parameters.

Since their introduction to cosmology over two decades ago, Fisher Information matrices have been ubiquitously used to forecast the constraining power of future experiments (*e.g.* Jungman et al. 1996; Tegmark et al. 1997; Dodelson 2003; Heavens 2009; Verde 2010). Defined as

$$F_{ij} = -\left\langle \frac{\partial^2 \ln\mathcal{L}}{\partial\theta_i \partial\theta_j} \right\rangle, \tag{8}$$

where $\mathcal{L}$ is the likelihood, the Fisher matrix for the bispectrum can be written as

$$F_{ij} = \frac{1}{2} \operatorname{Tr}\left[\boldsymbol{C}^{-1}\frac{\partial\boldsymbol{C}}{\partial\theta_i}\boldsymbol{C}^{-1}\frac{\partial\boldsymbol{C}}{\partial\theta_j} + \boldsymbol{C}^{-1}\left(\frac{\partial\overline{B}_0}{\partial\theta_i}\frac{\partial\overline{B}_0}{\partial\theta_j}^T + \frac{\partial\overline{B}_0}{\partial\theta_i}^T\frac{\partial\overline{B}_0}{\partial\theta_j} \right) \right]. \tag{9}$$

Since we assume that the B_0 likelihood is Gaussian, including the first term in Eq. 9 runs the risk of incorrectly including information from the covariance already included in the mean (Carron 2013).

We, therefore, conservatively neglect the first term and calculate the Fisher matrix,

$$F_{ij} = \frac{1}{2} \operatorname{Tr} \left[\boldsymbol{C}^{-1} \left(\frac{\partial \overline{B}_0}{\partial \theta_i} \frac{\partial \overline{B}_0}{\partial \theta_j}^T + \frac{\partial \overline{B}_0}{\partial \theta_i}^T \frac{\partial \overline{B}_0}{\partial \theta_j} \right) \right], \tag{10}$$

directly with $\boldsymbol{C}$ and $\partial B_0 / \partial \theta_i$ along each cosmological parameter from the Quijote simulations. For $\Omega_{\rm m}$, $\Omega_{\rm b}$, h, n_s, and σ_8, we calculate

$$\frac{\partial \overline{B}_0}{\partial \theta_i} \approx \frac{\overline{B}_0(\theta_i^+) - \overline{B}_0(\theta_i^-)}{\theta_i^+ - \theta_i^-}. \tag{11}$$

Meanwhile, for $\sum m_\nu$, where the fiducial value is 0.0 eV and we cannot have negative $\sum m_\nu$, we use the Quijote simulations at $\sum m_\nu^+, \sum m_\nu^{++}, \sum m_\nu^{+++} = 0.1, 0.2, 0.4$ eV (Table 1) to compute:

$$\frac{\partial \overline{B}_0}{\partial \sum m_\nu} \approx \frac{-21\overline{B}_0(\sum m_\nu^{\rm fid}) + 32\overline{B}_0(\sum m_\nu^+) - 12\overline{B}_0(\sum m_\nu^{++}) + \overline{B}_0(\sum m_\nu^{+++})}{1.2}. \tag{12}$$

By using these N-body simulations, instead of analytic methods (*e.g.* perturbation theory), we exploit the accuracy of numerical simulations in the nonlinear regime and rely on fewer assumptions and approximations. **CH:** something about quanity the information content of the bispectrum in the non-linear regime unprecedented. We discuss subtle details of the bispectrum derivatives in Appendix B and discuss tests of convegence in Appendix C.

We present the constraints on $\sum m_\nu$ and other cosmological parameters $\{\Omega_{\rm m}, \Omega_{\rm b}, h, n_s, \sigma_8\}$ derived from the redshift-space halo bispectrum Fisher matrix (Eq. 10) in Figure 7. For comparison, we include Fisher constraints of the parameters for the redshift-space halo power spectrum monopole in blue. The contours mark the 68% and 95% confidence interals. For both the power spectrum and bispectrum, we set $k_{\rm max} = 0.5$ h/Mpc. We also include in our Fisher cosntraints, parameters b', a free amplitude scaling factor, and $M_{\rm min}$, the halo mass limit. These parameters serve as a simplistic bias model and by marginalizing over them we ensure that our Fisher constraints do not include extra constraining power from the difference in bias/number density in the different Quijote cosmologies used to calculate $\partial \overline{B}_0 / \partial \theta_i$. b' is a multiplicative factor so $\partial \overline{B}_0 / \partial b' = \overline{B}_0$. Meanwhile, we numerically estimate $\partial \overline{B}_0 / \partial M_{\rm min}$ using $\overline{B}_0$ evaluated at $M_{\rm min}$=3.3 and $3.1 \times 10^{13} h^{-1} M_\odot$, with all other parameters fixed. In Table 2, we list the parameter constraints for $P_0(k < k_{\rm max} = 0.5$ h/Mpc$)$ and $B_0(k_1, k_2, k_3 < k_{\rm max} = 0.5$ h/Mpc$)$.

The bispectrum substantially improves constraints on all of the parameters over the power spectrum (Figure 7 and Table 2). More precisely, the bispectrum improves the marginalized $\Omega_{\rm m}$, $\Omega_{\rm b}$, h, n_s, and σ_8 constraints by factors of $\sim$4, 11, 10, 10, and 3 with respect to their power spectrum constraints. *For $\sum m_\nu$, the bispectrum improves the constraint from $\sigma_{\sum m_\nu} = 0.319$ to 0.0239 eV — over an order of magnitude improvement over the power spectrum.*

Even at lower $k_{\rm max} < 0.5$ h/Mpc, the bispectrum significantly improves cosmological parameter constraints. We compare the marginalized 1σ constraints of $\Omega_{\rm m}$, $\Omega_{\rm b}$, h, n_s, σ_8, and $\sum m_\nu$ as a function of $k_{\rm max}$ for B_0 (orange) and P_0 (blue) in Figure 8. **CH:** write this once we have to updated powerspectrum calculations.

discussing the results

- emphasize that this is only for a 1 Gpc box so our constraints will be so much better

- how does the bispectrum do so much better? — *i.e.* triangles that contribute most fisher information

- redshift-space helps us out (refer to appendix)

The results above definitively show that the bispectrum has significant constraining power in the weakly nonlinear regime ($k > 0.1\,h/\text{Mpc}$) beyond the power spectrum. Our results also demonstrated the potential of the bispectrum in constraining $\sum m_\nu$ (an order of magnitude improvement over P_0). Below, we underline a few caveats of the results we present above. First, the parameter constraints were derived using the Fisher matrix. This assumes

- mention the caveats of fisher forecasts

- emphasize the lack of bananas in the contours

- convergence concerns (refer to appendix)

- $\sum m_\nu$ dependence of derivatives along $\sum m_\nu$. (refer to appendix)

- take Fisher forecasts with a grain of salt

Another caveat is that our parameter constraints were derived using the power spectrum and bispectrum of halo in a periodic box. We do not consider a realistic survey geometry or radial selection function. A realistic selection function will smooth out the triangle configuration dependence and consequently degrade the constraining power of the bispectrum. In Sefusatti & Scoccimarro (2005), for instance, they find that the signal-to-noise of the bispectrum is significantly reduced once survey geometry is included in their forecast. Survey geometry, however, also degrade the signal-to-noise of their power spectrum forecasts. Hence, with the order of magnitude improve in the $\sum m_\nu$ constraining power of the bispectrum, even with survey geometry, including the bispectrum will improve $\sum m_\nu$ constraints.

Although we focus on the halo bispectrum and power spectrum in this paper, constraints on $\sum m_\nu$ will ultimately be derived from the distribution of galaxies. Besides the cosmological parameters, bias and nuisance parameters that allow us to marginalize over the galaxy—halo connection need to be incorporated to forecast $\sum m_\nu$ and other cosmological parameter constraints for the galaxy bispectrum. Although we include a *naive* bias model through b' and M_{min}, this is insufficient to describe how galaxies occupy halos. A more realistic bias model such as a halo occupation distribution (HOD) model involve extra parameters that describe the distribution of central and satellite galaxies in halos (*e.g.* Zheng et al. 2005; Leauthaud et al. 2012; Tinker et al. 2013; Zentner et al. 2016; Vakili & Hahn 2019). **CH:** maybe something about Uros and Nick's model involving a lot of parameters. Marginalizing over these extra parameters, will likely reduce the constraining power at high k. Even if the constraining power at high k is reduced, the bispectrum still offers significant improvements over the power spectrum at $k_{\text{max}} \sim 0.2$. Jointly analyzing power spectrum and bispectrum will help constrain these extra bias parameters. Furthermore, we again emphasize that the constraints we
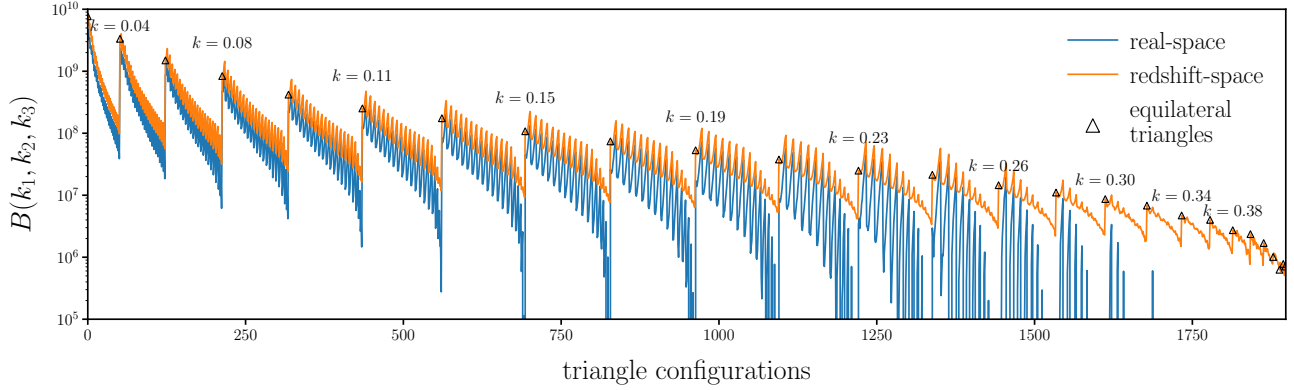
Figure 9. Comparison of the fiducial HADES simuluations real and redshift-space halo bispectrum for triangle configurations with $k_1, k_2, k_3 \leq k_{\max} = 0.5h/\text{Mpc}$ (blue and orange respectively). We mark equilateral triangle configurations (empty triangle marker) along with their side lengths k.

present in this paper is for a $1h^{-1}\text{Gpc}$ box. In Hahn et al. (in preparation), we will include a realistic HOD model and quantify the information content and constraining power of a joint galaxy power spectrum and bispectrum analysis.

5. SUMMARY

ACKNOWLEDGEMENTS

APPENDIX

A. REDSHIFT-SPACE BISPECTRUM

B. FISHER FORECAST DERIVATIVES

here's how we take derivatives

C. TESTING CONVERGENCE

REFERENCES

Ade, P. a. R., Aghanim, N., Arnaud, M., et al. 2016, Astronomy & Astrophysics, 594, A13

Angulo, R. E., & Pontzen, A. 2016, Monthly Notices of the Royal Astronomical Society, 462, L1

Brandbyge, J., Hannestad, S., Haugbølle, T., & Thomsen, B. 2008, Journal of Cosmology and Astro-Particle Physics, 08, 020

Carron, J. 2013, Astronomy & Astrophysics, 551, A88

Castorina, E., Sefusatti, E., Sheth, R. K., Villaescusa-Navarro, F., & Viel, M. 2014, Journal of Cosmology and Astro-Particle Physics, 02, 049

Davis, M., Efstathiou, G., Frenk, C. S., & White, S. D. M. 1985, The Astrophysical Journal, 292, 371

Dodelson, S. 2003, Modern Cosmology

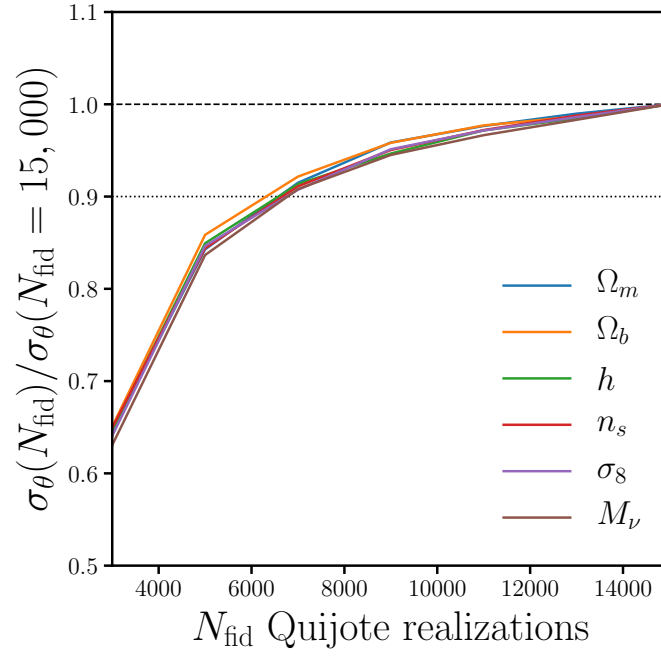Heavens, A. 2009, arXiv:0906.0664 [astro-ph], arXiv:0906.0664 [astro-ph]

Figure 10.

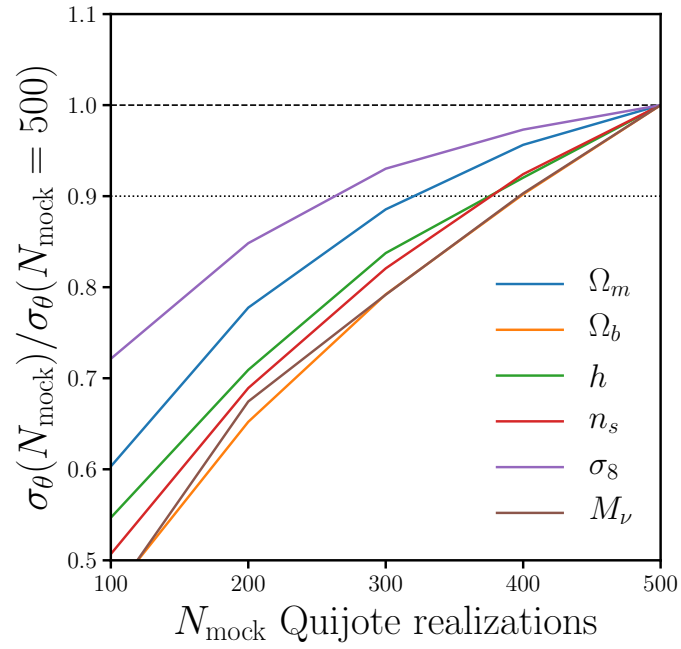**Figure 11.**

Hockney, R. W., & Eastwood, J. W. 1981, Computer Simulation Using Particles

Ichiki, K., & Takada, M. 2012, Physical Review D, 85, 063521

Jungman, G., Kamionkowski, M., Kosowsky, A., & Spergel, D. N. 1996, Physical Review D, 54, 1332

Leauthaud, A., Tinker, J., Bundy, K., et al. 2012, The Astrophysical Journal, 744, 159

LoVerde, M. 2014, Physical Review D, 90, 083518

Pontzen, A., Slosar, A., Roth, N., & Peiris, H. V. 2016, Physical Review D, 93, 103519

Scoccimarro, R. 2015, Physical Review D, 92, arXiv:1506.02729

Sefusatti, E., Crocce, M., Scoccimarro, R., & Couchman, H. M. P. 2016, Monthly Notices of the Royal Astronomical Society, 460, 3624

Sefusatti, E., & Scoccimarro, R. 2005, Physical Review D, 71, arXiv:astro-ph/0412626

Springel, V. 2005, Monthly Notices of the Royal Astronomical Society, 364, 1105

Tegmark, M., Taylor, A. N., & Heavens, A. F. 1997, The Astrophysical Journal, 480, 22

Tinker, J. L., Leauthaud, A., Bundy, K., et al. 2013, The Astrophysical Journal, 778, 93

Vakili, M., & Hahn, C. 2019, The Astrophysical Journal, 872, 115

Verde, L. 2010, arXiv:0911.3105 [astro-ph], 800, 147

Viel, M., Haehnelt, M. G., & Springel, V. 2010, Journal of Cosmology and Astro-Particle Physics, 06, 015

Villaescusa-Navarro, F., Banerjee, A., Dalal, N., et al. 2018, The Astrophysical Journal, 861, 53

Villaescusa-Navarro, F., Marulli, F., Viel, M., et al. 2014, Journal of Cosmology and Astro-Particle Physics, 03, 011

Zennaro, M., Bel, J., Villaescusa-Navarro, F., et al. 2017, Monthly Notices of the Royal Astronomical Society, 466, 3244

Zentner, A. R., Hearin, A., van den Bosch, F. C., Lange, J. U., & Villarreal, A. 2016, arXiv:1606.07817 [astro-ph], arXiv:1606.07817 [astro-ph]

Zheng, Z., Berlind, A. A., Weinberg, D. H., et al. 2005, The Astrophysical Journal, 633, 791